Research Square

Preprints are preliminary reports that have not undergone peer review.
They should not be considered conclusive, used to inform clinical practice,
or referenced by the media as validated information.

Reactive diboride redirects phase evolution towards hierarchical ordering in a multicomponent alloy

Qingjun Chen

q.jchen@nchu.edu.cn

Nanchang Hangkong University https://orcid.org/0000-0002-2833-3865

Yuting Wang

Nanchang Hangkong University

Li Ji

Nanchang Hangkong University

Xinwen Yang

Nanchang Hangkong University

Article

Keywords:

Posted Date: November 12th, 2026

DOI: https://doi.org/10.21203/rs.3.rs-11370237/v1

License: This work is licensed under a Creative Commons Attribution 4.0 International License.
Read Full License

Additional Declarations: There is **NO** Competing Interest.

Reactive diboride redirects phase evolution towards hierarchical ordering in a multicomponent alloy

Yuting Wang, Qingjun Chen*, Li Ji & Xinwen Yang

School of Materials Science and Engineering, Nanchang Hangkong University, Nanchang 330063, China

Corresponding author: Qingjun Chen, E-mail: qjchen@nchu.edu.cn

Abstract: Trace ceramic additions can redirect phase selection in multicomponent alloys. We introduce a nominal 0.05 wt% TiB_2 addition via an Al–TiB_2 master alloy into $Fe_{35}Co_{30}Ni_{25}Al_7Nb_3$ (at.%) and compare it with a base-composition-matched control under identical heat treatment. The cast processed state contains AlB_2-type $(Nb,Ti)B_2$ and substantially coarser FCC grains. After solution treatment and ageing, the processed alloy retains a continuous FCC matrix with $L1_2$ precipitates, interfacial B2 and B2 laths, whereas the control remains FCC-dominant. It reaches 1,209.5 ± 48.3 MPa tensile strength and 37.64 ± 1.61% total elongation (mean ± s.d., n = 3), with renewed work hardening. The measured $L1_2$ geometry yields an Orowan-form scale of approximately 356 MPa, far above the adopted-coefficient Hall–Petch estimate of 46.4 MPa. These findings associate a reaction-modified cast precursor with hierarchical ordering and a high strength–ductility response.

Introduction

Multicomponent alloys provide a versatile platform for developing structural materials through compositional complexity, local chemical heterogeneity and phase engineering.[1–3] Heterogeneous and metastable architectures can mitigate the strength–ductility trade-off by distributing deformation across phases and length scales.[4,5] In face-centred cubic (FCC)-based multicomponent alloys, ordered secondary phases are widely used to raise strength while retaining tensile ductility.[6,7,8,9,1011] Coupled or hierarchical ordered-phase architectures—including $L1_2$/B2 and related multicomponent intermetallic populations—extend this strategy beyond a single precipitate family.[12,13,14,15] Nevertheless, controlling when and where these ordered phases form remains challenging because most approaches rely on changing bulk alloy composition or the thermal path.

Ceramic additions offer another means of modifying alloy microstructures. TiB_2-bearing routes are usually discussed in terms of heterogeneous nucleation, grain refinement, Zener pinning

or particle-related strengthening.[16,17,18,19,20] Solidification, however, reflects competition among nucleation and growth processes,[21,22] and AlB_2-type transition-metal diborides can accommodate several metallic species, including Ti and Nb.[23,24,25,26] Interactions between an introduced diboride-bearing master alloy and a chemically complex melt may therefore create local chemistries distinct from those expected for an inert reinforcement. Such changes could modify the cast precursor and, in turn, the ordered phases observed after heat treatment; distinguishing particle reaction from Ti/B alloying and solute redistribution requires explicit controls.

An important unresolved issue is whether trace diboride-bearing additions can modify the development of ordered phases in multicomponent alloys under otherwise identical thermal treatments. In particular, the relationship between diboride-modified solidification microstructures, subsequent precipitation behaviour and mechanical response remains poorly understood. Several mechanisms could contribute to such changes, including local solute redistribution associated with boride formation, altered nucleation conditions and modified precipitation kinetics. Distinguishing among these possibilities is essential because they imply different pathways for controlling phase evolution. Furthermore, whereas ceramic-induced grain refinement is conventionally considered beneficial for strengthening, it remains unclear whether a diboride-bearing addition can promote a favourable strength–ductility response through changes in phase constitution and ordering even when grain refinement does not occur. Understanding these relationships could provide a distinct perspective on the use of trace additions for microstructural design in compositionally complex alloys.

Here, we investigate the influence of a nominal 0.05 wt% TiB_2 addition, introduced through an Al–TiB_2 master alloy, on the microstructural evolution and tensile behaviour of $Fe_{35}Co_{30}Ni_{25}Al_7Nb_3$ (at.%) multicomponent alloy. By comparing diboride-free and diboride-processed alloys in the as-cast state and after an identical solution-treatment and ageing schedule, we identify pronounced differences in their microstructural development and mechanical response. The diboride-processed cast alloy contains AlB_2-type Nb/Ti-containing borides and exhibits markedly coarser FCC grains in the examined regions. Following the common heat treatment, the processed alloy develops a hierarchical microstructure comprising an FCC matrix, $L1_2$ precipitates, interfacial B2 regions and discrete B2 laths in the analysed regions, whereas the corresponding control remains FCC-dominant. This microstructural architecture is accompanied by an ultimate tensile strength of 1,209.5 ± 48.3 MPa and a total elongation of 37.64 ± 1.61%, together with a renewed post-yield work-hardening response. These findings reveal an association between

diboride-bearing processing, the observed cast precursor, subsequent ordered-phase development and tensile performance.

Results

Trace diboride processing is associated with a high-strength, high-elongation response

The experimental design compares the nominal diboride-bearing addition under a common heat treatment (Fig. 1a). HEA and HEC-5 denote the as-cast TiB_2-free and nominally 0.05 wt% TiB_2-containing alloys, respectively; the suffix STA denotes solution treatment at 1,200 °C for 20 min followed by ageing at 750 °C for 1 h. The Al introduced with the Al–TiB_2 master alloy was included in the charge balance, so both alloys retained the nominal $Fe_{35}Co_{30}Ni_{25}Al_7Nb_3$ (at.%) base composition.

The four states exhibit distinct room-temperature engineering stress–strain responses (Fig. 1b). The representative as-cast HEA curve reaches approximately 810 MPa UTS and 5.5% total elongation; the specimen-level HEA mean is 789.1 ± 48.7 MPa and 7.08 ± 0.78% (mean ± sample s.d., n = 3 specimens). HEC-5-STA reaches 1,209.5 ± 48.3 MPa UTS and 37.64 ± 1.61% total elongation (mean ± sample s.d., n = 3 specimens). A representative HEC-5-STA fracture surface contains abundant dimples at higher magnification (Fig. 1c,d), consistent with substantial plastic deformation before final rupture.

The literature comparison in Fig. 1f uses selected processing states from five source studies spanning several alloy families and routes.[9,27,28,29,30] The dashed guide denotes PSE = 4×10^4 MPa%. Because source articles use different elongation definitions, the comparison is descriptive rather than a strict rank ordering. Within the present dataset, specimen-level mean PSE values are 0.561 ± 0.094, 2.158 ± 0.151, 2.432 ± 0.087 and 4.548 ± 0.093 × 10^4 MPa% for HEA, HEC-5, HEA-STA and HEC-5-STA, respectively (n = 3 specimens per state). Thus, heat treatment changes PSE by +334% in HEA and +111% in HEC-5, whereas the nominal addition changes PSE by +285% in the as-cast state and +87.0% after heat treatment. These descriptive contrasts preserve the four-state design and avoid attributing the confounded HEA-to-HEC-5-STA diagonal comparison to a single intervention.

Diboride-bearing processing restructures the as-cast precursor

In the displayed electron backscatter diffraction (EBSD) fields, HEC-5 is not a particle-refined

version of HEA. The mean FCC grain size increases from 18.03 μm in HEA to 263.06 μm in HEC-5; the corresponding medians are 9.3 and 210.1 μm, a factor of approximately 22.6 (Fig. 2a–c and Supplementary Table 1). The displayed HEC-5 map contains 14 coarse grains, whereas the HEA distribution contains 523 measured grains. The sampled regions therefore show a solidification outcome opposite to conventional grain refinement.

Transmission electron microscopy identifies a second, chemical signature of this change. HEC-5 contains 200–300 nm particles whose diffraction is consistent with an AlB_2-type structure (Fig. 2d–g and Supplementary Fig. 1). Elemental maps show local B, Nb and Ti enrichment within the analysed particles. At the indicated particle, energy-dispersive X-ray spectroscopy gives 54.8 at.% B, 37.2 at.% Nb and 3.0 at.% Ti, compared with 0.1 at.% B, 3.8 at.% Nb and 0.1 at.% Ti in the adjacent FCC matrix (Fig. 2f,h). Diffraction and lattice imaging support assignment of the analysed particle as AlB_2-type $(Nb,Ti)B_2$ rather than unchanged TiB_2, while the EDS data provide supporting evidence for local Nb/Ti/B enrichment.[23–26]

The co-occurrence of an AlB_2-type Nb/Ti-containing diboride and a roughly 15-fold shift in mean FCC grain size is consistent with a reaction-associated change in the cast precursor. HEC-5 therefore enters solution treatment with different grain dimensions and with locally observed Nb/Ti/B partitioning between analysed boride particles and the adjacent FCC matrix.

A common heat treatment produces different ordered-phase architectures

The common solution-treatment and ageing schedule produces sharply different phase architectures in the TEM regions examined (Fig. 3b–g). HEA-STA remains FCC-dominant in the analysed regions (Fig. 3b), whereas HEC-5-STA contains $L1_2$ precipitates and B2 regions inside a continuous FCC matrix (Fig. 3c–g). Under matched thermal conditions, this contrast is associated with the different cast precursor rather than with a different ageing schedule.

The ordered phases occur in two coupled topologies. B2 locally decorates or envelops leaf-shaped $L1_2$ precipitates, producing an interfacial $L1_2$/B2 configuration (Fig. 3c–e). Elsewhere, B2 forms discrete laths without an identifiable $L1_2$ core (Fig. 3f,g). Fast Fourier transforms and selected-area electron diffraction distinguish the FCC, $L1_2$ and B2 order, and local diffraction gives an approximate $[\bar{1}11]B2 \parallel [110]FCC$ zone-axis parallelism (Fig. 3h). Point-EDS measurements further resolve compositional differences among FCC matrix, B2-rich and mixed B2/$L1_2$ regions (Fig. 3i).

The $L1_2$ population has a measured edge-to-edge spacing of 168 ± 76 nm (n = 63

measurements) and an equivalent circular diameter of 270.8 ± 73.9 nm (n = 126 precipitates), obtained from two TEM fields (Fig. 3j,k). Together, the continuous FCC matrix, dispersed $L1_2$ precipitates, interfacial B2 and discrete B2 laths define a hierarchy in both length scale and phase topology. The essential observed contrast is phase selection: under the same thermal path, the analysed HEA-STA regions remain FCC-dominant, whereas the analysed HEC-5-STA regions contain an FCC/$L1_2$/B2 architecture.

HEC-5-STA exhibits renewed post-yield hardening

Conversion of the engineering curves to true stress and true strain exposes the deformation response behind the high UTS–elongation combination (Fig. 4a). HEC-5-STA continues to carry increasing true stress over a broad strain interval, whereas HEC-5 loses load-bearing capacity at a lower stress and strain. After the initial post-yield decrease, the work-hardening rate of HEC-5-STA recovers near 1% true strain and reaches a broad maximum around 3%; the HEC-5 rate instead continues to fall after its early maximum (Fig. 4b). The recovered hardening interval is consistent with sustained strain accommodation after the high-strength state has been established, as reported for other precipitation-strengthened concentrated alloys.[31,32,33]

Undeformed EBSD maps provide spatial context for the two states before tensile loading (Fig. 4c–f). The native-step KAM maps (Fig. 4c,d) and corresponding software-exported geometrically necessary dislocation (GND)-density maps (Fig. 4e,f) show local orientation-gradient heterogeneity in HEC-5 and HEC-5-STA. The maps were acquired at step sizes of 3 μm and 2 μm, respectively, so their native-step KAM and GND magnitudes are not directly comparable between states. Cross-field summaries calculated on a common 6 μm grid are provided in Supplementary Fig. 2d–f and Supplementary Table 2.

The undeformed EBSD maps do not independently identify the dislocation processes during tensile loading. Their spatial variations are presented descriptively; quantitative cross-field comparison requires the common-grid analysis reported in Supplementary Fig. 2d–f and Supplementary Table 2. The direct mechanical evidence for renewed post-yield strain hardening remains the tensile response (Fig. 4a,b).

Measured precipitate geometry defines a larger model stress scale than the grain-boundary estimate

The sampled HEC-5 and HEC-5-STA regions contain coarse grains, so these local

microstructures do not support a conventional grain-refinement explanation of the mechanical response. Using a common Hall–Petch coefficient adopted from single-phase FCC $Al_{0.3}CoCrFeNi$, the measured mean FCC grain sizes give estimated grain-boundary stress scales of 194.1, 201.8, 50.8 and 46.4 MPa for HEA, HEA-STA, HEC-5 and HEC-5-STA, respectively (Fig. 5a). These values are model estimates rather than material-specific measurements of the Hall–Petch contribution.

The measured $L1_2$ geometry provides a larger model stress scale. The XRD-refined FCC lattice parameter of HEC-5-STA is 0.3621 nm, giving a Burgers-vector magnitude of 0.2560 nm. With an $L1_2$ equivalent diameter of 270.8 nm and edge-to-edge spacing of 168 nm, an Orowan-form relation gives a characteristic stress scale of approximately 356 MPa (Fig. 5b). Spacing dominates the sensitivity: changing λ from 92 to 244 nm at fixed diameter changes the calculated scale from 651 to 245 MPa, whereas changing the diameter from 196.9 to 344.7 nm at fixed spacing changes it from 338 to 370 MPa (Fig. 5c).

These estimates compare two experimentally anchored length-scale-based stress scales; they are not a complete additive reconstruction of the tensile curve and do not establish a unique dislocation–precipitate interaction mechanism. Within the adopted parameter set, HEC-5-STA has an Orowan-form $L1_2$ stress scale of approximately 356 MPa and an estimated Hall–Petch scale of 46.4 MPa. Contributions from B2, solid-solution strengthening, interfacial constraint and deformation heterogeneity cannot be independently quantified from the present measurements.

Discussion

This study identifies an unconventional route by which a trace ceramic addition modifies a multicomponent alloy: diboride-bearing processing is associated with a chemically modified cast microstructure rather than an unambiguously inert particle addition. The analysed borides in as-cast HEC-5 are AlB_2-type $(Nb,Ti)B_2$, enriched to 37.2 at.% Nb against 3.8 at.% in the adjacent matrix, although the addition supplies TiB_2. AlB_2-type diborides tolerate extensive metal substitution,[23,24,25,26] so dissolution, elemental exchange and reprecipitation are possible explanations for the observed Nb-containing borides, although the reaction sequence was not directly observed. Such chemical modification could affect the nucleation and pinning roles often ascribed to TiB_2 particles,16–20 consistent with the approximately 15-fold difference in mean grain size between the sampled HEC-5 and HEA fields. Solidification is governed by competition between nucleation and growth,[21,22] but the specific nucleation and growth processes responsible

for the observed contrast remain unresolved.

The altered cast precursor is associated with the different microstructures obtained after the common heat treatment. After identical solution treatment and ageing, the control alloy remains FCC-dominant, whereas the processed alloy develops $L1_2$ precipitates wrapped by interfacial B2, together with discrete B2 laths, inside a continuous FCC matrix. Local Nb/B partitioning and the coarse-grained cast structure are possible contributors to this divergence, but the available final-state measurements do not establish their separate causal roles. The interfacial topology, in which B2 decorates or envelops leaf-shaped $L1_2$, suggests a spatial relationship between B2 and $L1_2$, without establishing the precipitation sequence. Coupled $L1_2$/B2 populations are an established route to strength–ductility synergy in concentrated alloys;[12,13,14,15,34,35] the present architecture shows that they can be obtained through the cast precursor rather than through bulk composition or a specialized thermal path.[36]

The same hierarchy accounts for the mechanical response. With a mean grain size of 315.25 μm, the adopted-coefficient Hall–Petch scale is only 46.4 MPa, whereas the measured $L1_2$ geometry sets an Orowan-form scale of approximately 356 MPa; the ordered precipitates may therefore provide a substantial strengthening contribution, although the two model stress scales do not establish a unique mechanism. The ductility rests on how the hierarchy deforms. The work-hardening rate recovers near 1% true strain and peaks again around 3%, a signature of sustained strain accommodation reported in other precipitation-strengthened concentrated alloys,[31,32] and consistent with deformation being distributed across the FCC matrix, the $L1_2$ population and the two B2 topologies instead of localizing at one interface family.4,5 The outcome is a coarse-grained alloy that combines 1,209.5 MPa ultimate strength with 37.64% elongation, a strength–elongation product of 4.548×10^4 MPa%. Achieving this response without grain refinement reverses the usual logic of ceramic additions, in which the ceramic is expected to refine the grains and the refinement is expected to provide the strengthening.[37]

Alternative explanations can be ranked against this mechanism. Direct strengthening by boride particles alone is unlikely to account for the entire response: the analysed particles are sparse 200–300 nm features, and the high strength–ductility response appears only after ageing, once the hierarchical architecture exists. Grain refinement through heterogeneous nucleation or Zener pinning, the standard account of TiB_2 additions,[16,17,18,19,20] predicts the opposite of the observed coarsening. A subtler alternative is microalloying, because the master alloy introduces Ti and B together with the diboride; separating a solute effect from particle reaction requires a diboride-free

Ti/B-only control, although the (Nb,Ti)B_2 chemistry already excludes a purely inert addition. Three kinetic routes could each translate the precursor into the aged architecture: local solute redistribution, altered nucleation conditions and modified precipitation kinetics. The present measurements associate the architecture with the precursor but do not discriminate among these routes, and the distinction is practical, because each route implies a different lever for controlling phase selection.

Three boundaries delimit these conclusions. The microstructural statistics are field-level, with 14 coarse HEC-5 grains against 523 HEA grains and seven EBSD fields across the four states, so the coarsening claim covers the sampled regions rather than whole ingots. The stress scales are model estimates built on coefficients adopted from $Al_{0.3}CoCrFeNi$, so the comparison between 356 MPa and 46.4 MPa ranks strengthening channels without decomposing the measured yield stress; the B2, solid-solution and interfacial contributions remain unquantified. The reaction pathway itself was not observed in situ. The discriminating experiments follow directly: diboride-free Ti/B-only controls to isolate the reaction, interrupted solidification to capture it and post-deformation electron microscopy to resolve how dislocations interact with the $L1_2$/B2 topology. If these tests confirm the reaction pathway, trace diboride-bearing master alloys would offer a route to hierarchical ordering that leaves the base composition of a multicomponent alloy untouched.

Methods

Material preparation

Alloys were prepared by vacuum arc melting under high-purity argon from Fe, Co, Ni, Al and Nb (>99.9 wt%) and an Al–TiB_2 master alloy containing 85 wt% Al and 15 wt% TiB_2. The Al supplied by the master alloy was included in the charge calculation, and elemental Al was reduced correspondingly to retain the nominal $Fe_{35}Co_{30}Ni_{25}Al_7Nb_3$ (at.%) base composition. Each ingot was inverted and remelted at least five times to improve compositional homogeneity. The TiB_2-free alloy is denoted HEA; the alloy containing Ti and B introduced through a nominal 0.05 wt% TiB_2 addition is denoted HEC-5.

As-cast specimens were solution treated at 1,200 °C for 20 min and aged at 750 °C for 1 h. Both stages used a heating rate of 10 °C min^{-1} and were followed by water quenching. The suffix STA denotes the solution-treated and aged states, HEA-STA and HEC-5-STA.

Microstructural characterization

Phase constitution and FCC lattice parameters were determined by X-ray diffraction using Cu Kα radiation over 2θ = 20–100° for the scans at a scan rate of 0.5° s^{-1} and Rietveld refinement (Fig. 3a).[38] Microstructures were examined by scanning electron microscopy (JSM-7100F) and transmission electron microscopy (FEI Talos F200X). TEM foils were prepared by conventional ion-beam thinning. Local chemistry and crystallography were assessed by energy-dispersive X-ray spectroscopy (EDS), selected-area electron diffraction (SAED), fast Fourier transforms (FFT) and high-resolution TEM.

Grain sizes and orientations were measured by EBSD.[39,40] Kernel average misorientation was calculated from raw FCC orientations with a first-order eight-neighbour kernel, a 5° neighbour cutoff and at least three valid neighbours. For the common-grid cross-field comparison in Supplementary Table 2, the KAM-derived GND-density proxy was calculated as

$$\rho = \frac{2\theta}{hb} \qquad (1)$$

where θ is KAM in radians, h is the analysis step and b is the FCC Burgers-vector magnitude. The condition-specific value of b was calculated from the XRD-refined lattice parameter as

$$b = \frac{a_{FCC}}{\sqrt{2}} \qquad (2)$$

giving b = 0.2556, 0.2543, 0.2551 and 0.2560 nm for HEA, HEA-STA, HEC-5 and HEC-5-STA, respectively. The native-step EBSD fields in Fig. 4c–f were acquired at 3 μm for HEC-5 and 2 μm for HEC-5-STA. Fig. 4e,f show software-exported FCC GND-density maps (½〈110〉 convention, α = 3); these native-step maps are distinct from the separately recomputed common-grid KAM-derived GND proxies. The common-grid KAM-derived GND-density proxies in Supplementary Table 2 use Eq. (1) with a fixed b = 0.2528 nm. Six macroscale fields were analysed on a common 6 μm grid for Supplementary Fig. 2d–f and Supplementary Table 2; a 0.05 μm HEC-5-STA microfield was analysed at its native step.

Thermodynamic calculations

Equilibrium phase fractions for nominal $Fe_{35}Co_{30}Ni_{25}Al_7Nb_3$ (at.%) were calculated with Thermo-Calc 2025 and the TCHEA8 database. The calculated phase landscape was used to select the 1,200 °C solution-treatment and 750 °C ageing temperatures. The calculation used the nominal

Ti/B-free base composition and excluded reaction-generated local chemical heterogeneity; it was not intended to predict the precipitation sequence or local chemistry of HEC-5 (Supplementary Note 2, Supplementary Table 3 and Supplementary Fig. 3).

Room-temperature tensile testing

Uniaxial tensile tests were performed at room temperature with an Instron 5969 machine at an initial strain rate of 1×10^{-3} s^{-1}. Polished dog-bone specimens had a 6.5 mm × 2 mm × 1.2 mm gauge section, and engineering strain was measured using an extensometer. Tensile specimens were machined without a prescribed orientation relative to the ingot. The 0.2% offset yield strength was determined from engineering stress–strain data by interpolation or extrapolation. Three separate specimens were tested for each condition. UTS and total elongation are reported as mean ± sample s.d.

Engineering stress–strain curves were converted using $\sigma_t = \sigma_{eng}(1 + \varepsilon_{eng})$ and $\varepsilon_t = \ln(1 + \varepsilon_{eng})$, where σ_{eng} and ε_{eng} are engineering stress and engineering strain, respectively. Duplicate data points were removed, and the true-stress–true-strain data were smoothed in Origin (OriginLab) using a first-order Savitzky–Golay filter with a 51-point window before a single numerical differentiation was performed to calculate the work-hardening rate, $\Theta = d\sigma_t/d\varepsilon_t$. For each specimen, the strength–elongation product was calculated from its paired values as PSE = UTS × total elongation (%). State-level PSE is reported as the mean ± sample s.d. of the three specimen products; the change between states was calculated from their mean PSE values as $\Delta PSE = (PSE_{after} - PSE_{initial})/PSE_{initial} \times 100\%$. Literature comparison points retain the elongation definitions used by the source studies.[9,27,28,29,30]

Strengthening-scale calculations

The Hall–Petch and Orowan calculations compare two experimentally anchored stress scales from the measured grain size and $L1_2$ geometry; they are not treated as a complete additive strength model.[41,42,43] Grain-boundary strengthening was calculated as

$$\Delta\sigma_{HP} = k_y d^{\frac{-1}{2}} \quad (3)$$

where d is the measured mean FCC grain size. The coefficient k_γ = 824 MPa $\mu m^{1/2}$ was adopted from single-phase FCC $Al_{0.3}CoCrFeNi$.[44] For d = 18.03, 16.67, 263.06 and 315.25 μm, the calculated terms are 194.1, 201.8, 50.8 and 46.4 MPa for HEA, HEA-STA, HEC-5 and HEC-5-STA, respectively.

The $L1_2$ particle stress scale was estimated with the Orowan bypass relation

$$\Delta\sigma_{Or} = M\frac{0.4Gb}{\pi\sqrt{1-\nu}}\frac{ln\left(\frac{r_p}{b}\right)}{\lambda} \quad (4)$$

where M is the Taylor factor, G the matrix shear modulus, ν Poisson's ratio, b the FCC Burgers-vector magnitude, r_p the precipitate radius and λ the measured edge-to-edge spacing. For HEC-5-STA, the measured values are d_p = 270.8 ± 73.9 nm and λ = 168 ± 76 nm. Values of M = 3.06, G = 80 GPa and ν = 0.30 were adopted from an FCC $Al_{0.3}$CoCrFeNi analysis using the same parameters in an Orowan calculation.[45] With b = 0.2560 nm, d_p = 270.8 nm and λ = 168 nm, Eq. (4) gives approximately 356 MPa. The sensitivity values in Fig. 5c use the measured mean ± s.d. limits for diameter and spacing.

Statistics and reproducibility

$L1_2$ diameter and spacing statistics were obtained from two TEM fields of view (n = 126 precipitates for diameter and n = 63 measurements for spacing). Grain-size distributions contain 523 measured grains for HEA and 14 for the displayed HEC-5 dataset. EBSD orientation-gradient summaries are reported at the field level in Supplementary Table 2. Seven EBSD fields were available across the four states; six macroscale fields were analysed on a common 6 μm grid, and one HEC-5-STA microfield was analysed at its native 0.05 μm step (Supplementary Table 2). Field identifiers denote acquisition fields, not independently prepared ingots (Supplementary Note 1). Tensile UTS, total elongation and specimen-level PSE are reported as mean ± sample s.d. from three separate specimens per condition; the number of independent ingots represented by these tensile specimens was not established. No blinding or randomization was used.

Generative AI-assisted manuscript preparation

OpenAI ChatGPT and Codex were used to assist manuscript organization and language editing. The authors are responsible for the scientific interpretations, calculations, references and final wording.

Data availability

The data that support the findings of this study are available from the corresponding author upon reasonable request.

References

1. Zhang, M., Zhang, B., Ding, J. & Ma, E. Quantifying the local compositional fluctuation and Shannon entropy inherent in multi-principal element alloys. Scr. Mater. 259, 116559 (2025).
2. Cantor, B. Multicomponent high-entropy Cantor alloys. Prog. Mater. Sci. 120, 100754 (2021).
3. Li, W. et al. Mechanical behavior of high-entropy alloys. Prog. Mater. Sci. 118, 100777 (2021).
4. Li, Z., Pradeep, K. G., Deng, Y., Raabe, D. & Tasan, C. C. Metastable high-entropy dual-phase alloys overcome the strength–ductility trade-off. Nature 534, 227–230 (2016).
5. Ma, E. & Wu, X. Tailoring heterogeneities in high-entropy alloys to promote strength–ductility synergy. Nat. Commun. 10, 5623 (2019).
6. Lu, W., Wang, Y., Luo, X., Huang, B. & Yang, Y. A $L1_2$ precipitation strengthened Co-free medium-entropy alloy with superior high-temperature performance. Intermetallics 162, 108031 (2023).
7. Fang, J. et al. Competition between continuous and discontinuous precipitation in $L1_2$-strengthened high-entropy alloys. Intermetallics 149, 107655 (2022).
8. Yang, Y. et al. Bifunctional nanoprecipitates strengthen and ductilize a medium-entropy alloy. Nature 595, 245–249 (2021).
9. Wang, Z. et al. Effect of coherent $L1_2$ nanoprecipitates on the tensile behavior of a fcc-based high-entropy alloy. Mater. Sci. Eng. A 696, 503–510 (2017).
10. Liang, Y.-J. et al. High-content ductile coherent nanoprecipitates achieve ultrastrong high-entropy alloys. Nat. Commun. 9, 4063 (2018).
11. Li, W. et al. Unraveling the two-stage precipitation mechanism in a hierarchical-structured fcc/$L2_1$ high-entropy alloy: experiments and analytical modeling. Acta Mater. 262, 119426 (2024).
12. Wang, L. et al. Synergistic $L1_2$ and B2 co-precipitation enabled by high Ti and Al additions for strength-ductility synergy in a heterostructured CoNiCr medium-entropy alloy. Intermetallics 192, 109231 (2026).
13. Ming, K., Bi, X. & Wang, J. Realizing strength-ductility combination of coarse-grained $Al_{0.2}Co_{1.5}CrFeNi_{1.5}Ti_{0.3}$ alloy via nano-sized, coherent precipitates. Int. J. Plast. 100, 177–191 (2018).
14. Li, L. et al. Strengthening and toughening of the $Co_{34}Cr_{32}Ni_{27}Al_{3.5}Ti_{3.5}$ alloy through coherent $L1_2$ nanoprecipitates. Adv. Eng. Mater. 26, 2302111 (2024).
15. Yang, T. et al. Multicomponent intermetallic nanoparticles and superb mechanical behaviors of complex alloys. Science 362, 933–937 (2018).
16. Kumar, D., Seetharam, R. & Ponappa, K. A review on microstructures, mechanical properties and processing of high entropy alloys reinforced composite materials. J. Alloys Compd. 972, 172732 (2024).
17. Zhai, W., Zhou, W. & Nai, S. M. L. Achieving submicron grains in additively manufactured 304L–TiB_2 metal matrix composite via in-situ reaction and Zener pinning. Mater. Sci. Eng. A 951, 149497 (2026).
18. Wang, Y. L., Zhao, L., Wan, D., Guan, S. & Chan, K. C. Additive manufacturing of TiB_2-containing CoCrFeMnNi high-entropy alloy matrix composites with high density and enhanced mechanical properties. Mater. Sci. Eng. A 825, 141871 (2021).

19. Zhang, C., Zhu, J., Zhang, G. & Hu, Y. Laser powder bed fusion of nano-TiB_2 reinforced FeCoNiCr high-entropy alloy with enhanced strength and firm corrosion resistance. J. Alloys Compd. 927, 167110 (2022).
20. Zhang, Z., Yan, S. & Qin, Q. Additive manufacturing of nano-TiB_2 particles reinforced CrCoNi medium-entropy alloy matrix composites with high strength and ductility. J. Alloys Compd. 1043, 184323 (2025).
21. Gao, F. & Fan, Z. Competition for nucleation and grain initiation during solidification. Metals 12, 1512 (2022).
22. Balasubramani, N. et al. Investigating the grain refinement mechanisms of pulsed electric current, ultrasonic and melt stirring solidification of pure aluminium. JOM 73, 3873–3882 (2021).
23. Monteverde, F., Cassese, S., De Prisco, D., Mungiguerra, S. & Savino, R. Searching the limits of compositionally complex AlB_2-type diboride solid solutions for hypersonic applications. J. Eur. Ceram. Soc. 46, 118206 (2026).
24. Feng, L., Monteverde, F., Fahrenholtz, W. G. & Hilmas, G. E. Superhard high-entropy AlB_2-type diboride ceramics. Scr. Mater. 199, 113855 (2021).
25. Potanin, A. et al. Combustion synthesis and hot pressing of the $(Ti,Nb)B_2$–(Ti,Nb)C solid-solution ceramics with near-eutectic composition. J. Eur. Ceram. Soc. 46, 118689 (2026).
26. Vedel, D. et al. Conditions for the formation of a solid solution in the $(Ti,Zr,Hf)B_2$, $(Zr,Hf,Nb)B_2$ and $(Zr,Hf,Ta)B_2$ systems. Mater. Sci. 60, 684–691 (2025).
27. Xiong, T., Zheng, S., Pang, J. & Ma, X. High-strength and high-ductility $AlCoCrFeNi_{2.1}$ eutectic high-entropy alloy achieved via precipitation strengthening in a heterogeneous structure. Scr. Mater. 186, 336–340 (2020).
28. Bhattacharjee, T. et al. Simultaneous strength–ductility enhancement of a nano-lamellar $AlCoCrFeNi_{2.1}$ eutectic high entropy alloy by cryo-rolling and annealing. Sci. Rep. 8, 3276 (2018).
29. He, L. et al. Selective laser melting of dense and crack-free $AlCoCrFeNi_{2.1}$ eutectic high entropy alloy: synergizing strength and ductility. J. Mater. Sci. Technol. 117, 133–145 (2022).
30. Xu, L. et al. Dual precipitate simultaneous enhancement of tensile and fatigue strength in $(FeCoNi)_{86}Al_7Ti_7$ high-entropy alloy fabricated using selective laser melting. J. Mater. Sci. Technol. 148, 90–104 (2023).
31. Lu, W. et al. γ″ phase transformation, precipitation hardening, hetero-deformation induced hardening and deformation mechanisms in a Nb-alloyed medium-entropy alloy. Mater. Des. 225, 111477 (2023).
32. Chang, H. et al. Strengthening and strain hardening mechanisms in precipitation-hardened CrCoNi medium entropy alloys. J. Alloys Compd. 896, 162962 (2022).
33. He, Q., Yoshida, S. & Tsuji, N. Unique work-hardening behavior and dislocation microstructure evolution in HfNbTiZr refractory medium-entropy alloy. Mater. Sci. Eng. A 950, 149514 (2026).
34. Li, Q. et al. Pulsed electric-induced synergistic strengthening in metastable dual-phase $CoCrFeNiAl_{0.5}$ high-entropy alloy overcomes the strength-ductility trade-off. Mater. Sci. Eng. A 944, 148931 (2025).
35. Zhu, J. et al. Quad-heterostructure precipitation-strengthened high-entropy alloy overcomes strength-ductility trade-off from cryogenic to intermediate temperatures. Mater. Res. Lett. 13, 411–419 (2025).
36. Wang, N. et al. Laser-directed energy deposition-induced hierarchical multiscale microstructures with in situ $L1_2$ nanoprecipitates and core–shell structures in a medium-entropy alloy. Rare Met. 45, e70307 (2026).

37. Jie, D., Wu, M., Miao, X. & Kim, H. S. TiN mediated heterostructured nanoprecipitates enable strength-ductility synergy in laser cladding FeMnCoCr metastable high entropy alloy. Mater. Res. Lett. 14, 1309–1318 (2026).
38. Toby, B. H. A simple solution to the Rietveld refinement recipe problem. J. Appl. Crystallogr. 57, 175–180 (2024).
39. Zhao, C. & Li, X. Quantitative study of residual strain and geometrically necessary dislocation density using HR-EBSD method. Exp. Mech. 61, 1281–1290 (2021).
40. Wiesman, H. S. & Wallis, D. The effect of pattern quality on measurements of stress heterogeneity and geometrically necessary dislocation density by high-angular resolution electron backscatter diffraction. Ultramicroscopy 282, 114330 (2026).
41. Chen, J. et al. Tailoring concentrations of principal elements to promote Hall–Petch strengthening of NiCoCrFe high entropy alloys. Intermetallics 187, 108999 (2025).
42. Jagetia, A. et al. Ordering-mediated local nano-clustering results in unusually large Hall–Petch strengthening coefficients in high entropy alloys. Mater. Res. Lett. 9, 213–222 (2021).
43. Thirathipviwat, P. et al. A role of atomic size misfit in lattice distortion and solid solution strengthening of TiNbHfTaZr high entropy alloy system. Scr. Mater. 210, 114470 (2022).
44. Gwalani, B. et al. Optimizing the coupled effects of Hall–Petch and precipitation strengthening in a $Al_{0.3}$CoCrFeNi high entropy alloy. Mater. Des. 121, 254–260 (2017).
45. Wang, X., Zhang, Z., Wang, Z. & Ren, X. Microstructural evolution and tensile properties of $Al_{0.3}$CoCrFeNi high-entropy alloy associated with B2 precipitates. Materials 15, 1215 (2022).

Acknowledgements

This work was supported by the Jiangxi Province 2030 Qihang Program, Class A (grant no. 20262AAC270004). The authors thank Dalian Ketian New Materials Co., Ltd. for support.

Author contributions

Yuting Wang conceived the project and wrote the manuscript. Qingjun Chen supervised the project and analysed the data. Li Ji coordinated alloy ingot melting. Xinwen Yang prepared the samples. All authors discussed the results and approved the final manuscript.

Competing interests

The authors declare no competing interests.

Figure legends

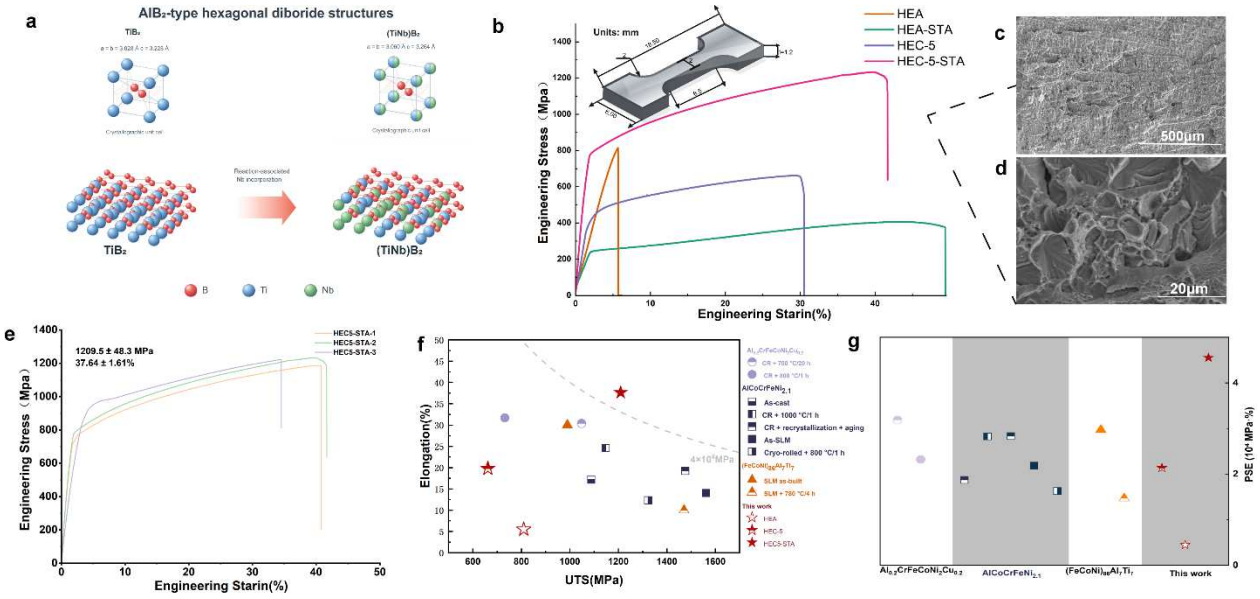


Fig. 1 Diboride-bearing processing is associated with a modified cast precursor and distinct strength–elongation responses. a, Crystal-structure models and a reaction-associated hypothesis contrasting AlB_2-type TiB_2 with Nb-substituted $(Nb,Ti)B_2$; the pathway was not monitored in situ. b, Representative room-temperature engineering stress–strain curves for HEA, HEA-STA, HEC-5 and HEC-5-STA; inset, tensile-specimen geometry (dimensions in mm). c,d, Representative low- and high-magnification fracture surfaces of HEC-5-STA (scale bars, 500 μm and 20 μm). e, Engineering stress–strain curves for three HEC-5-STA specimens. The aggregate UTS and total elongation are 1,209.5 ± 48.3 MPa and 37.64 ± 1.61%, respectively (mean ± sample s.d., n = 3 specimens). f, UTS versus reported elongation for three present-study entries (HEC-5, HEA and HEC-5-STA; red stars) and selected literature processing states.[9,27–30] The dashed curve denotes PSE = 4 × 10^4 MPa%; literature elongation definitions follow the source articles, so the comparison is descriptive. g, PSE for the same source-data entries, grouped by alloy family and plotted in units of 10^4 MPa%. PSE = UTS × reported elongation. For the present study, state-level PSE is the mean of three specimen-level products (n = 3 specimens per state).

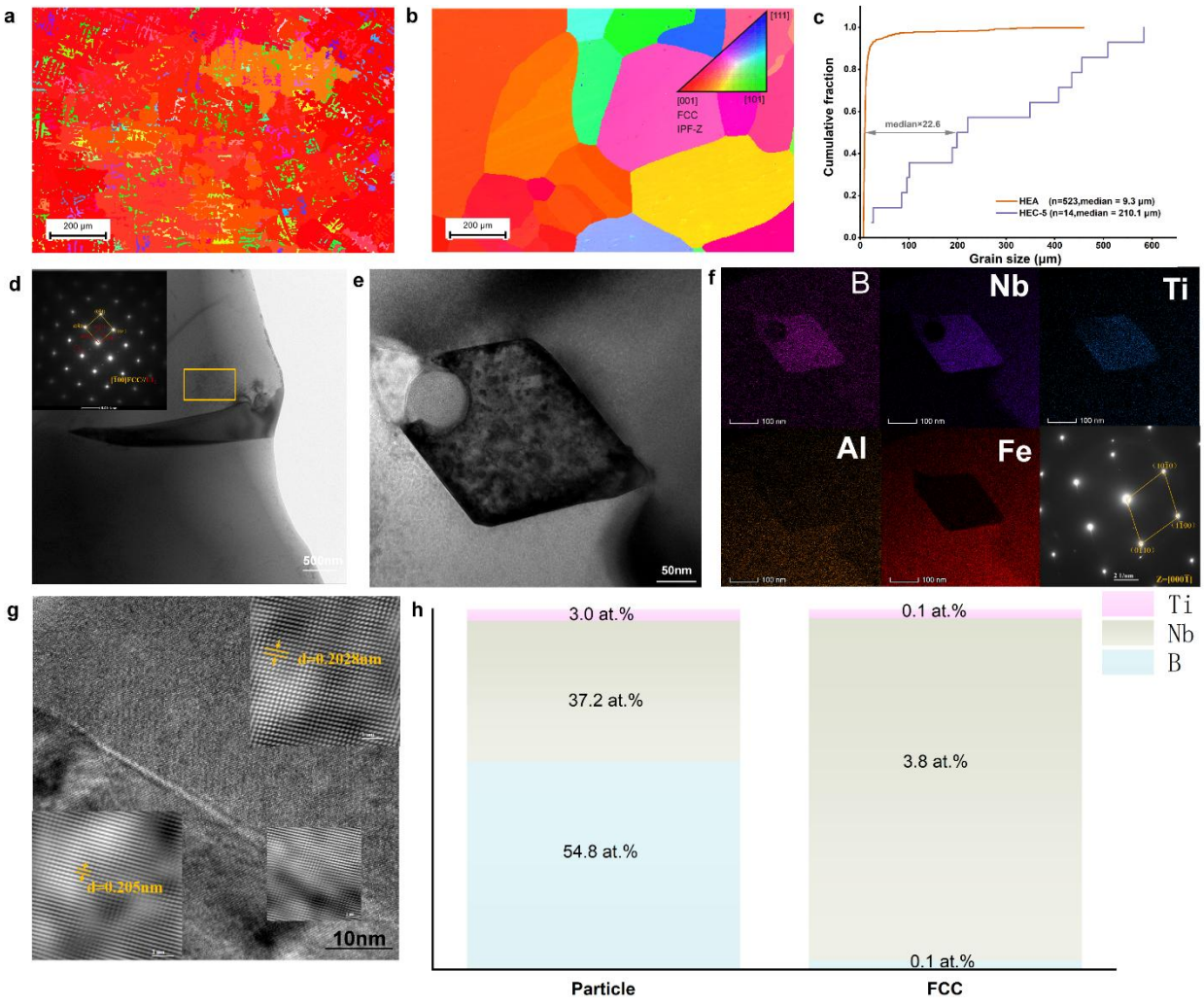


Fig. 2 Trace diboride processing coarsens the FCC matrix and is associated with AlB_2-type $(Nb,Ti)B_2$ formation. a,b, FCC inverse-pole-figure maps of HEA and HEC-5, respectively. c, Cumulative grain-size distributions; n denotes counted grains and arrows mark median values. d,e, Bright-field TEM images of an analysed boride particle in HEC-5; inset in d, local diffraction from the adjacent FCC matrix. f, STEM-EDS maps of B, Nb, Ti, Al and Fe and diffraction from the particle. g, HRTEM image of the particle/FCC interface with lattice-fringe measurements. h, Local EDS compositions for the particle and adjacent FCC matrix.

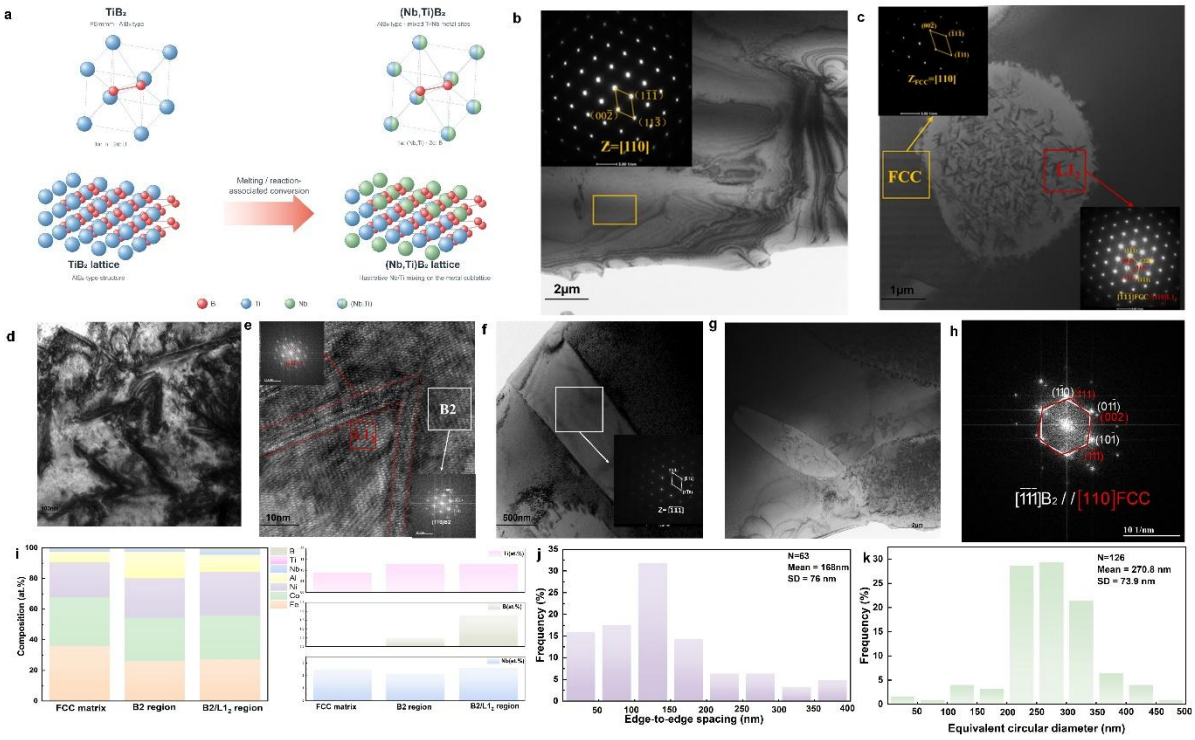


Fig. 3 The diboride-processed precursor develops hierarchical FCC/L1₂/B2 ordering under the common heat treatment. a, X-ray diffraction patterns and Rietveld refinements for HEA, HEA-STA, HEC-5 and HEC-5-STA, including refined FCC lattice parameters. b, Representative TEM image and diffraction from an FCC-dominant HEA-STA region. c–e, FCC/L1₂/B2 regions in HEC-5-STA, including interfacial or enveloping B2 adjacent to L1₂; insets show local diffraction or FFTs. f,g, Discrete B2 laths in the FCC matrix. h, Local diffraction showing approximate [$\bar{1}$11]B2 ∥ [110]FCC zone-axis parallelism. i, Point-EDS compositions at the indicated FCC matrix, B2-rich and mixed B2/L1₂ regions. j,k, L1₂ edge-to-edge spacing and equivalent-circular-diameter distributions, respectively. Values are mean ± s.d.; n = 63 spacing measurements and n = 126 precipitates for diameter from two TEM fields.

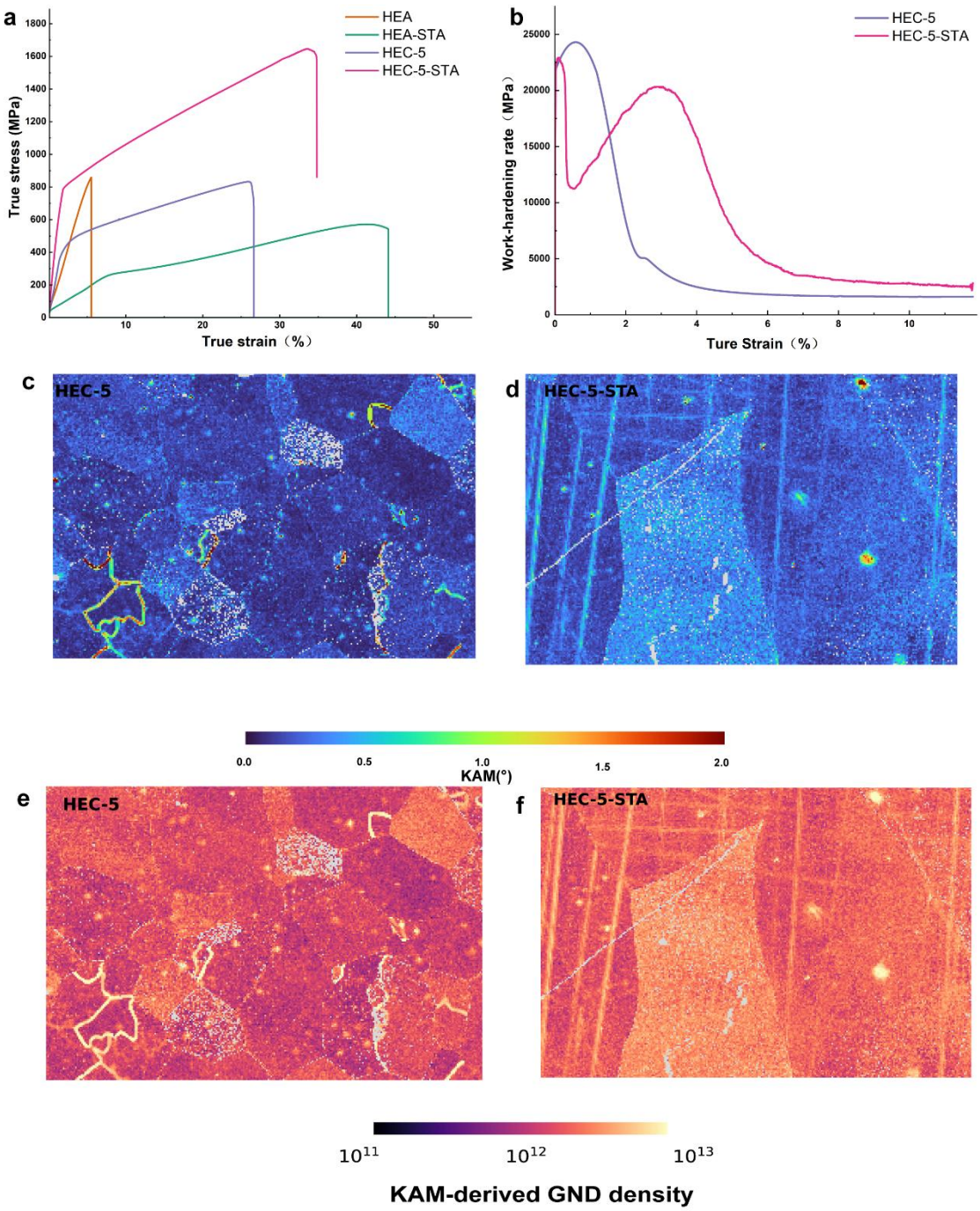


Fig. 4 HEC-5-STA exhibits renewed work hardening and spatial variation in undeformed orientation gradients. a, True stress versus true strain for the four conditions. b, Work-hardening rate versus true strain for HEC-5 and HEC-5-STA; duplicate data points were removed, the data were smoothed in Origin using a first-order Savitzky–Golay filter with a 51-point window, and then a single numerical differentiation was performed. c,d, Native-step KAM maps of undeformed HEC-5 and HEC-5-STA, acquired at 3 and 2 μm, respectively. e,f, Corresponding

GND-density maps exported directly from the EBSD analysis software for the same fields, rather than the separately recomputed KAM-derived GND-density proxies presented in the Supplementary Information. Different EBSD acquisition steps preclude direct quantitative comparison of these native-step maps; common-grid cross-field summaries are reported in Supplementary Fig. 2d–f and Supplementary Table 2.

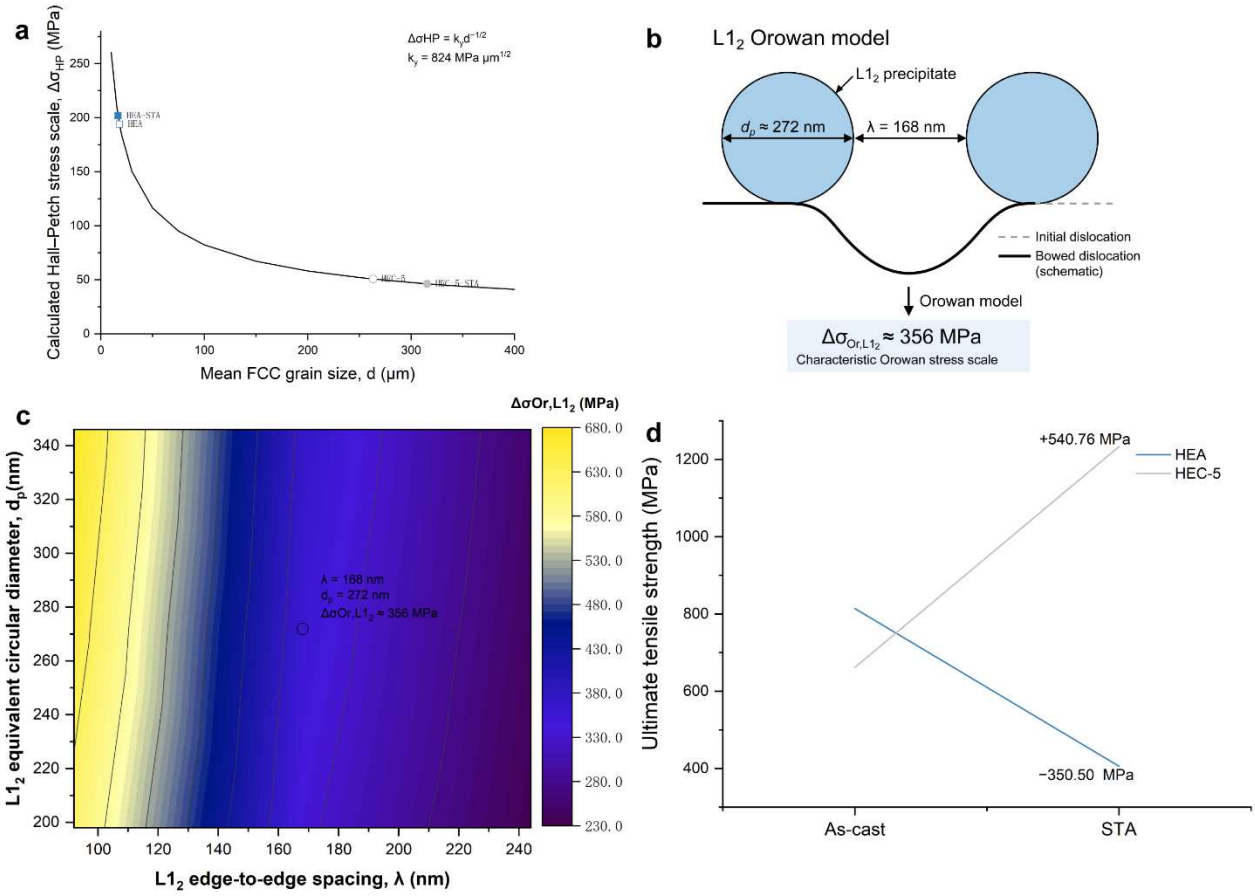


Fig. 5 Measured length scales give a larger L1₂ Orowan-form stress scale than the adopted Hall–Petch estimate. a, Hall–Petch stress scales estimated from measured mean FCC grain sizes for HEA, HEA-STA, HEC-5 and HEC-5-STA using the adopted coefficient reported in Methods; open and filled symbols denote as-cast and solution-treated-and-aged states. b, Orowan-form schematic and characteristic L1₂ stress scale for HEC-5-STA using d_p = 270.8 nm, λ = 168 nm and the parameters reported in Methods. c, Sensitivity of the Orowan-form stress scale to the measured mean ± s.d. limits of L1₂ spacing and diameter.

Supplementary Files

This is a list of supplementary files associated with this preprint. Click to download.

- supplement.pdf